

Supplementary Materials for

Lense–Thirring frame dragging induced by a fast-rotating white dwarf in a binary pulsar system

V. Venkatraman Krishnan*, M. Bailes, W. van Straten, N. Wex, P. C. C. Freire, E. F. Keane, T. M. Tauris, P. A. Rosado, N. D. R. Bhat, C. Flynn, A. Jameson, S. Osłowski

*Corresponding author. Email: vkrishnan@mpifr-bonn.mpg.de

Published 31 January 2020, *Science* **367**, 577 (2020)
DOI: [10.1126/science.aax7007](https://doi.org/10.1126/science.aax7007)

This PDF file includes:

Materials and Methods

Figs. S1 to S11

Table S1

References

Materials and Methods

Data recording The data from the Parkes telescope were taken with the central beam of the Parkes 21 cm “multibeam” receiver (29) using 6 different backends over the years 2000–2018. The backends used were the Analog Filterbank System (AFB), Caltech Parkes Swinburne Recorder 2 (CPSR2), three Parkes Digital Filterbanks (PDFB1, PDFB2, PDFB3) and The Collaboration for Astronomy Signal Processing and Electronics Research- CASPER Parkes Swinburne Recorder (CASPSR) (see (30) for details of the backends). The data from the UTMOST telescope were recorded using the The Molonglo Pulsar Swinburne Recorder (MOPSR) backend (20). The data recording used the DSPSR (31) and PSRCHIVE (18) software packages which in turn used the TEMPO2 (32) pulsar timing analysis software to obtain phase predictors to fold the data at the topocentric period of the pulsar.

Figure S4 provides an overview of the data reduction pipeline for Parkes. The data reduction for PSR J1141–6545 was performed using two different polarisation calibration techniques: the Measurement Equation Template Matching (METM) technique (33) and the Invariant Interval (34) to check for consistency between the ToAs. The millisecond pulsar PSR J0437–4715(Right Ascension= $04^h37^m15.8^s$, Declination = $-47^\circ15'09.1''$; Epoch=J2000) was used as the polarisation reference source for METM calibrations. The data from PSR J1141–6545 and PSR J0437–4715 were first integrated up to T_{int} seconds (usually 180 seconds) and subjected to a median radio frequency interference (RFI) filter. Reference noise-diode observations for the flux and polarisation calibration were passed through a calibration filter which used a baseline estimation algorithm to filter out RFI prone calibration observations. The data were then flux calibrated using observations of the Hydra radio galaxy (Right Ascension= $09^h18^m05.651^s$, Declination= $-12^\circ05'43.99''$, Epoch=J2000) and then polarisation calibrated. The Invariant Interval data were obtained from the METM calibrated data by taking the invariant component

($I_{inv} = \sqrt{I^2 - (Q^2 + U^2 + V^2)}$) where I , Q , U , and V are the Stokes parameters (9) of the pulse profile (9), after accounting for accurate rotation measure (RM) corrections. Temporally evolving analytical standard templates were then obtained for each calibration model using an empirical profile evolution model. These standard templates were then used to obtain the Times of Arrival (ToA) of the pulses. The ToAs from the calibration and the Invariant Interval technique were cross checked and were found to agree within the uncertainties. The rest of the analysis was then performed with the METM ToAs. The ToAs were then subjected to a Bayesian red-noise and pulsar parameter estimator (TEMPONEST; (35)) from which estimates of pulsar parameters were obtained. The pulsar parameters also included relevant parameters for a glitch in its rotation that occurred at MJD ~ 54272.7 , also reported in (36). Major steps in the pipeline are detailed below. The pipeline for UTMOST data reduction is provided in (37).

Polarimetric Calibration Incomplete polarimetric calibration usually results in a systematic change to the total intensity profile (38). In the case of PSR J1141–6545, it also resulted in contamination of the orbital parameters, given the ~ 4.8 -hour orbital period of the system spanning a wide range of parallactic angles in the usual full-orbit observing modes undertaken at the Parkes radio telescope. To mitigate such contaminations, polarimetric calibration was carried out using the METM technique (33) that uses a combination of measurement equation modelling (38, *MEM*) and matrix template matching (39, *MTM*). This technique used regular observations of a millisecond pulsar, PSR J0437–4715 over a wide range of parallactic angle to obtain the instrumental response of the 20-cm multibeam receiver and its variations over time. Only observations that had corresponding robust calibration solutions (with a reduced $\chi^2 < 1.2$) were chosen for further analysis. We used the PSRPL data reduction pipeline which is part of the PSRCHIVE package (18) for this analysis.

Evolving pulsar profiles Temporal evolution of the pulse profile width and amplitude meant that we could not use a single standard template to obtain ToAs, as this could result in systematic long-term timing drifts that are co-variant with the physical parameters of interest. To combat this, we produced temporally evolving standard profiles parameterized by a set of von Mises distributions (cyclic-gaussian distributions; hereafter “components”).

Firstly, the number of components required to obtain a good approximation to the observed pulse profile was estimated. To do so, the observing epoch with the widest pulse profile was chosen and fit with a set of scaled von Mises distributions parameterized by a centroid (k) and a concentration (μ), with its probability density function taking the form $f(x|(\mu, k)) = e^{k \cos(x-\mu)}$. This differs from the original von Mises distribution by the scale factor $(1/(2\pi I_0(k)))$ where $I_0(k)$ is a zero-th order Bessel function. Components are iteratively added to the model until the fitting residuals were sufficiently like white-noise, as determined by the value of the on-pulse residual root-mean-square (RMS) statistic being similar to its off-pulse counterpart. For PSR J1141–6545, a set of 3 components ($C^i; \forall i = \{0, 1, 2\}$) was found to be a good approximation to the widest pulse profile in the dataset. The values (μ^i, k^i) and their corresponding amplitudes (heights; h^i), were stored as the initial model (M_{init}). The distribution whose centroid is closest to the flux-centroid of the total intensity profile was then chosen as the “primary” component (C_{init}^0). The relative phase-distances of the centroids of the other components from that of the primary component C_{init}^0 ($d^i = (k_{init}^i - k_{init}^0) \forall i = \{1, 2\}$) was then held fixed for the rest of the procedure.

For each observing epoch (E_j), the phase centre of the pulse (ϕ_j^c) was obtained by convolving the observation with the primary component. The primary component was then placed at ($k_j^0 = \phi_j^c$) while other components were introduced relative to the primary component, mediated by d^i . The concentration and the heights of all the components were then allowed to simultaneously vary and were fit to obtain updated values (μ_j^i, h_j^i) . k_j^i need not necessarily be k_{init}^i as

inaccuracies in the initial timing model will shift the absolute phase centre ϕ_j^c . To prevent this change being absorbed into the profile evolution model, a new model M_j was saved with the updated concentrations and heights (μ_j^i, h_j^i) but with the original centroids k_{init}^i . M_j . This was then used as the initial estimate for the next observing session E_{j+1} . This method assumes that ϕ_j^c was not modified by profile evolution itself (and may not be a good assumption for other pulsars) but given the timing precision of PSR J1141–6545, small changes to ϕ_j^c from profile evolution are negligible and are absorbed into the red noise model.

Once the corresponding models (M_j) for all epochs (E_j) were recorded, the temporal evolution of $(\mu_j^i, h_j^i) \forall C^i$ was fitted with a set of 5th degree polynomial functions $X^i = \{P_\mu^i, P_h^i\}$ to obtain a smooth evolution of each component model, so that any inaccuracies in Radio Frequency Interference (RFI) rejection or calibration skewing the pulse profile shape, did not affect the analytical standard. This empirical evolution model(X^i), was then used to create noise-free standard profiles (A_k^i), separated by 50 days each. Each observing epoch (E_j) was then timed with the standard profile that was closest in time to the observing epoch.

PAAS program in the PSRCHIVE package (18) was primarily used for this analysis. It was improved to accept additional keywords in the input “initial guess” model file such as “fix relative phases” to fix the centroids of the components at the same relative position with respect to the primary, “fit primary first” to fix the centroid of the primary component to the phase centre of the pulse before introducing other components, “set log heights” to force the height of the components to be positive and “return original phases” that makes the updated model return the new values for concentration and height but retain the input values for the centroids.

Estimates of red noise and pulsar parameters Slow pulsars such as PSR J1141–6545 have characteristic secular drifts in their timing residuals, thought to come from emission irregularities inherent to the pulsar. Such secular drifts, for long baseline timing analysis, can be

correlated with several parameters of interest and may lead to severe underestimation of the uncertainties of the pulsar parameters. To determine the uncertainties, a simultaneous model fitting for the red noise and the pulsar parameters is necessary. We use TEMPONEST (35), a Bayesian pulsar timing analysis software that uses TEMPO2 (32), the standard pulsar timing package and MULTINEST (40), a Bayesian inference tool, to perform a non-linear fit for the pulsar’s parameters and a red noise model combined with white-noise modifiers per backend system. These white-noise modifiers are time-independent noise sources parameterized by two values. Firstly an uncertainty factor (EFAC), which accounts for mis-calibrated radiometer noise in the system by multiplying the ToA uncertainties (σ_i) by a constant (E_f). Secondly, an uncertainty addition in quadrature (EQUAD), which accounts for the high frequency tail of the red noise spectrum by adding a constant (E_q) in quadrature to σ_i . The corrected uncertainty on each ToA can then be given as $\hat{\sigma}_i^2 = E_f \sigma_i^2 + E_q^2$ (this is the definition used in TEMPONEST which differs from its counterpart in TEMPO2). The red noise in the data is assumed to be a stationary, stochastic signal with a power-law spectrum whose spectral density $S(f)$ is given by $S(f) \propto A_{\text{red}}^2 f^{-\alpha_{\text{red}}}$ where f , A_{red} , and α_{red} are Fourier frequency, the red noise amplitude and the red noise spectral index, respectively.

Whilst temporal variations of the dispersion measure could also produce temporal drifts in the timing residuals, the variations are expected to be at a level that is negligible for a slow pulsar like PSR J1141–6545. Nevertheless, we attempted to model DM variations using the DM model defined in TEMPONEST. Fitting this model produced posterior pulsar parameters that are consistent with the values without the addition of this parameter, and a Bayesian Information Criterion (BIC) check strongly disfavoured the addition of this parameter ($\Delta BIC > 100$).

We use the TT(BIPM) clock correction procedure defined by the International Astronomical Union and computed by the Bureau International des Poids et Mesures (BIPM) and use DE436 solar system model for our computations. The post-fitting residuals is shown in Figure S5 and

the important parameter correlations in Figure S6.

Contributions to \dot{x}_{obs} In binary pulsar systems, the observed change in the projected semi-major axis of the pulsar orbit, \dot{x}_{obs} can arise due to a number of physical and geometric contributions, which can be decomposed as

$$\dot{x}_{\text{obs}} = \dot{x}_{\text{PM}} + \dot{x}_{\text{D}} + \dot{x}_{\text{GW}} + \dot{x}_{\dot{m}} + \dot{x}_{3^{\text{rd}}} + \dot{x}_{\dot{\epsilon}_A} + \dot{x}_{\text{SO}} \quad (\text{S1})$$

where the contributions are from the proper motion of the system (\dot{x}_{PM}), the changing radial Doppler shift (\dot{x}_{D}), gravitational wave (\dot{x}_{GW}) emission, mass-loss in the system ($\dot{x}_{\dot{m}}$), the presence of a hypothetical third body in the system ($\dot{x}_{3^{\text{rd}}}$), a secular change in the aberration of the pulsar beam due to geodetic precession ($\dot{x}_{\dot{\epsilon}_A}$), and spin-orbit (\dot{x}_{SO}) coupling (9). We examine each of these parameters in the following subsections.

Proper motion and changing Doppler shift The maximal contribution from \dot{x}_{PM} is given by

$$\dot{x}_{\text{PM}} \leq 1.54 \times 10^{-16} x \cot i \left(\frac{\mu_T}{\text{mas yr}^{-1}} \right) \quad (\text{S2})$$

where μ_T is the total proper motion on the sky (10, 12).

The contribution from the changing Doppler shift is given by

$$\dot{x}_{\text{D}} \sim x \left[\left(\frac{V_T^2}{dc} \right) + \frac{\vec{K}_0 \cdot (\vec{a}_{\text{PSR}} - \vec{a}_{\text{SSB}})}{c} \right] \quad (\text{S3})$$

where d is the distance to the pulsar and $V_T = \mu_T d$ is its corresponding transverse velocity, \vec{K}_0 is the unit vector from the Solar system barycentre to the pulsar and $(\vec{a}_{\text{PSR}} - \vec{a}_{\text{SSB}})$ is the differential Galactic acceleration of the pulsar with respect to the Solar system barycentre (10, 12).

We estimated the contributions of \dot{x}_{PM} and \dot{x}_{D} using a variety of measurements of the proper motion and the distance to the pulsar. Estimates of the proper motion were obtained from scintillation velocity measurements (41, 42). Firstly, the dispersion measure (DM) of the pulsar was

used along with two different Galactic electron density models (namely the NE2001 (43) and YMW16 (44)) to obtain distance estimates of 2.4 kpc and 1.6 kpc respectively. The neutral hydrogen absorption estimate of the lower limit to the distance is 3.7 kpc (45). A distance estimate from scintillation velocity measurements is $\sim 10_{-3}^{+4}$ kpc (42). Although these estimates are inconsistent, the maximum possible contributions of \dot{x}_{PM} and \dot{x}_{D} , by taking the most conservative distance estimate, was $\sim 2\%$ of \dot{x}_{obs} at most for each.

Gravitational wave emission We estimate the \dot{x}_{GW} contribution to \dot{x}_{obs} using the measured rate of change of the orbital period ($\dot{P}_{\text{b}}^{\text{obs}}$) which, for this exercise can be assumed to be the contribution to \dot{P}_{b} from gravitational wave emission ($\dot{P}_{\text{b}}^{\text{GW}}$), since

$$\frac{\dot{x}_{\text{GW}}}{x} = \frac{2}{3} \frac{\dot{P}_{\text{b}}^{\text{GW}}}{P_{\text{b}}} \simeq \frac{2}{3} \frac{\dot{P}_{\text{b}}^{\text{obs}}}{P_{\text{b}}}. \quad (\text{S4})$$

We find it to be of the order of $10^{-18} \text{ s s}^{-1}$. This is 5 orders of magnitude smaller than \dot{x}_{obs} . This term is hence negligible and is ignored in this analysis.

Mass loss in the system A mass loss from the system due to radiation emission from the neutron star and/or a wind from the companion would result in an additional contribution to the orbital period derivative, $\dot{P}_{\text{b}}^{\text{obs}}$. A limit for the contribution to \dot{x}_{obs} from mass loss in the system (\dot{x}_{m}) can then be obtained by using the residual observational uncertainty ($\Delta \dot{P}_{\text{b}}$) on $\dot{P}_{\text{b}}^{\text{obs}}$ after subtracting the contribution from $\dot{P}_{\text{b}}^{\text{GW}}$ (see (46), their eqs. (4.1) and (4.2))

$$\frac{\dot{x}_{\text{m}}}{x} = \frac{\dot{a}_{\text{m}}}{a} \sim \frac{\Delta \dot{P}_{\text{b}}}{P_{\text{b}}}, \quad (\text{S5})$$

where a denotes the semi-major axis of the relative orbit, and a_{m} its change due to mass loss. We find this contribution to be of the order of $10^{-19} \text{ s s}^{-1}$ which is 6 orders of magnitude lower than our detection. This term is hence negligible and is ignored in this analysis.

Presence of a hypothetical third body We rule out the presence of any hypothetical third body in our system as it should have resulted in contributions to the higher order frequency derivatives of the pulsar spin. Including higher order spin derivatives in our model fitting returned posterior distributions consistent with 0 and were also strongly disfavoured ($\Delta BIC > 20$).

Rate of change of aberration The orbital motion of the rotating pulsar causes the pulsar beam to be “aberrated” into a distant observer’s line of sight. The effects of aberration on pulsar timing are not separately measurable as they are completely absorbed as a redefinition of the Keplerian parameters (12). Such redefinitions, among others, also cause the observed projected length of the semi-major axis (x_{obs}) to differ from the intrinsic value ($x_{\text{intrinsic}}$) by a factor of $(1 + \epsilon_A)$, where ϵ_A is the first aberration parameter (A) divided by x (10). This aberration term depends on the pulsar spin period, the Keplerian parameters, and the system’s polar angles. In a spin-aligned system, this would mean that aberration can never be distinctly measured using pulsar timing alone. However, for misaligned systems such as PSR J1141–6545, geodetic precession gives rise to changes to the geometry of the system, and hence changes ϵ_A on timescale of the geodetic precession. This causes an apparent secular evolution of Keplerian parameters including the orbital eccentricity and projected semi-major axis, thus contributing to \dot{x}_{obs} .

The contribution to \dot{x}_{obs} from a change in the aberration due to the geodetic spin-precession of the pulsar ($\dot{x}_{\dot{\epsilon}_A}$) is given by

$$\dot{x}_{\dot{\epsilon}_A} = x \left(\frac{d\epsilon_A}{dt} \right) = -x \frac{P}{P_b} \frac{\Omega_{\text{geod}}}{(1 - e^2)^{1/2}} \frac{\cot \lambda_p \sin 2\eta_p + \cot i \cos \eta_p}{\sin \lambda_p} \quad (\text{S6})$$

(12, 47), where P_b is the orbital period, Ω_{geod} is the geodetic precession rate, λ_p is the angle between the pulsar spin and the line of sight, η_p is the longitude of precession (see Figure 1 and S1 for definitions of these and other angles). The contribution to \dot{x}_{obs} from the rate of change of aberration hence depends on the system’s geometry. The inclination angle was measured

using the DDGR timing model as $i = 71^\circ \pm 2^\circ$. An equally likely solution for i arising from symmetry, $(180^\circ - i) = 109^\circ \pm 2^\circ$, has been ruled out using measurements of the pulsar's scintillation velocity (42). While η_p mediates the sign of $\dot{x}_{\dot{\epsilon}_A}$, its absolute magnitude increases rapidly (see Figure S7) as λ_p approaches 0° (or 180°), meaning the pulsar's spin (or anti-spin) is very close to our line-of-sight. Hence it is necessary to constrain the ranges of λ_p and η_p .

An analysis of the evolving total intensity pulse profile (due to relativistic spin precession) was performed to understand the orientation and the geometry of the pulsar (19). Under the usual assumption of the circular beam model of pulsar emission, we set limits on λ_p of $66^\circ < \lambda_p < 114^\circ$, marginalizing over all other geometric evolutions, with 99% confidence (19). This shows that the contributions of $\dot{x}_{\dot{\epsilon}_A}$ from aberration is at most 20% of \dot{x}_{obs} . There are a number of other arguments to support this conclusion. Firstly, it is unlikely that the pulsar spin (or anti-spin) that is randomly oriented on the sky is close to our line of sight. Secondly, such a close alignment of the spin axis to our line of sight would make the pulsar a nearly-aligned rotator, while still possessing a narrow duty-cycle ($\sim 10\%$) across 20 years of precession (19, 36), which is also unlikely, as the near-alignment would require the pulsar's beam to be pointing towards the earth for most of its rotational phase. Thirdly, if we assume such a nearly-aligned orientation, and that \dot{x}_{obs} is entirely due to $\dot{\epsilon}_A$, there is another observable that should be detectable: the rate of change of observed eccentricity (\dot{e}). To first order, the predominant contributions to \dot{e} come from gravitational wave emission (\dot{e}_{GW}) and the rate of change of aberration ($\dot{e}_{\dot{\epsilon}_A}$). Neglecting the $\sim 10^{-18}$ contribution from \dot{e}_{GW} , the contributions from $\dot{\epsilon}_A$ to \dot{x}_{obs} and \dot{e}_{obs} are expected to be related as $\dot{x}_{\dot{\epsilon}_A}/x = \dot{e}_{\dot{\epsilon}_A}/e$. Consequently, if \dot{x}_{obs} is entirely due to $\dot{\epsilon}_A$, then we expect $\dot{e} \simeq (e/x)\dot{x}_{\text{obs}} \simeq 10^{-14} \text{ s}^{-1}$. To test this, we re-analyzed the data with an additional model parameter for \dot{e} . Our measured $\dot{e}_{\text{obs}} = (-2 \pm 8) \times 10^{-15} \text{ s}^{-1}$ is consistent with a non-detection, with its mean value that is below the expected detection level of $+1 \times 10^{-14} \text{ s}^{-1}$, for an \dot{x}_{obs} solely due to changing aberration. The large variance however, does not provide a stringent

constraint on the contribution to \dot{x}_{obs} from $\dot{\epsilon}_A$, although a constraint of $\dot{x}_{\dot{\epsilon}_A} < 0.4 \dot{x}_{\text{obs}}$ is obtained with 68% confidence. Additionally, a BIC check also strongly disfavors ($\Delta BIC \sim 10$) the addition of the extra model parameter. All the above arguments favour results derived from the pulsar's geodetic precession. A precession of the orbital plane due to spin-orbit interactions (\dot{x}_{SO}) should then provide the dominant contribution (> 79%) to \dot{x}_{obs} (see Figure S8).

Spin-orbit interaction from the white-dwarf The contribution of classical spin-orbit coupling (\dot{x}_{QPM}) due to the rotationally induced quadrupole moment of the white dwarf to \dot{x}_{obs} is given by:

$$\dot{x}_{\text{QPM}} = x \left(\frac{2\pi}{P_b} \right) Q \cot i \sin 2\delta_c \sin \Phi_c^0 \quad (\text{S7})$$

where

$$Q = \frac{k_2 R_c^2 \hat{\Omega}_c^2}{2a^2(1-e^2)^2} \quad \text{with} \quad \hat{\Omega}_c \equiv \frac{\Omega_c}{(Gm_c/R_c^3)^{1/2}} \quad (\text{S8})$$

and $\Omega_c = 2\pi/P_{\text{WD}}$ (48–50). For the radius of a $1.02 M_\odot$ white dwarf one finds $R_c \simeq 5400$ km (assuming WD to be an ideal degenerate Fermi gas (51)). The equation-of-state and composition independent I-Love-Q relations (52) for the WD were used to obtain $k_2 = 0.081$. Equation S7 includes only the contributions of spin-induced quadrupole moment. Contributions from tides and magnetic fields negligible and have been ignored.

The contribution to \dot{x}_{obs} from Lense-Thirring precession (\dot{x}_{LT}) due to the WD spin is given by

$$\dot{x}_{\text{LT}} \simeq -x \frac{GS_c}{c^2 a^3 (1-e^2)^{3/2}} \left(2 + \frac{3m_p}{2m_c} \right) \cot i \sin \delta_c \sin \Phi_c^0 \quad (\text{S9})$$

where $S_c = I_c \Omega_c$ is the WD angular momentum, with I_c being its moment of inertia (10).

MCMC simulations of spin-orbit coupling We perform MCMC simulations with the EMCEE software package (53) in the PYTHON programming language, and solve for equations

[S7](#) and [S9](#) simultaneously, to find the minimum WD spin period that could give rise to the spin-orbit coupling contributions to \dot{x}_{obs} , using uniform priors for the possible range of the angles $\{\delta_c, \Phi_c^0\}$. We use the Gelman-Rubin convergence criterion (54) to check the convergence of our MCMC chains implemented in the CHAINCONSUMER package (55). We marginalise over the dimensions $\{\delta_c, \Phi_c^0\}$ to obtain the minimum period of the WD, regardless of its orientation, along with the individual contributions of classical quadrupole and Lense-Thirring interactions.

Using the known values for M_c, R_c, I_c and k_2 in [S7](#) and [S9](#) we obtain the following simplified equations for the relative contributions from \dot{x}_{QPM} and \dot{x}_{LT} :

$$\dot{x}_{\text{QPM}} = 0.88 \times 10^{-13} (P_{\text{WD}}/5 \text{ min})^{-2} \sin 2\delta_c \sin \Phi_c^0, \quad (\text{S10})$$

$$\dot{x}_{\text{LT}} = -2.58 \times 10^{-13} (P_{\text{WD}}/5 \text{ min})^{-1} \sin \delta_c \sin \Phi_c^0. \quad (\text{S11})$$

It can be seen from these equations that \dot{x}_{QPM} and \dot{x}_{LT} contribute on the same order of magnitude to \dot{x}_{SO} if P_{WD} is a few minutes.

Contributions to $\dot{\omega}$ from spin-orbit interaction The spin-orbit interactions also result in contributions to the advance of periastron, whose magnitudes depend on angles $\{\delta_c, \Phi_c^0\}$ (50). We find that the present precision of $\dot{\omega}$ is insufficient to place any limit on the additional contribution from spin-orbit coupling and hence cannot be used to constrain the $\delta_c - \Phi_c^0$ parameter space. The contribution from the tidally induced quadrupole moment is at most $\sim 1\%$ of the spin induced contribution (56).

Consistency with binary evolution For our calculation of the evolution of a helium star-white dwarf (WD) binary, the progenitor system of PSR J1141–6545, we applied the BEC stellar evolution code, i.e. the “Langer code” (25, 26, 57–59). We assumed an initial helium star donor mass of $M_{\text{He}} = 2.9 M_{\odot}$, a WD mass of $M_{\text{WD}} = 0.96 M_{\odot}$ and an orbital period of 0.40 days. The WD mass and the orbital period were found by iteration until the post-Roche-lobe overflow (RLO) solution matched the present mass of the WD ($1.02 M_{\odot}$) and a pre-SN orbital period (0.14 days) in accordance with our SN analysis reproducing the PSR J1141–6545 system (see below).

Figure S9 shows the evolution of the helium-star donor in a Kippenhahn diagram, displaying the evolution of the internal structure of the star. We were unable to evolve the star until core collapse (mainly due to a rigorous helium shell flash (25)), but the core/envelope boundary and the total mass are frozen in that remaining short epoch (26). At the end of the RLO, the helium star has been stripped down to a pre-SN mass of only $1.58 M_{\odot}$ and a remaining helium envelope of about $0.06 M_{\odot}$. These are typical characteristics for ultra-stripped SNe (25–27). Given the relatively small mass of the resulting NS observed in the PSR J1141–6545 system ($1.27 M_{\odot}$), we expect a low kick velocity of $\sim 50 \text{ km s}^{-1}$ (60), producing a small misalignment angle of the WD spin axis with respect to the orbital angular momentum vector in the present system (see further discussions below on the effect of the SN).

Figure S10 shows the calculated mass-transfer rate as a function of time (since the helium star was on its zero-age main sequence) which is highly super-Eddington. The Eddington accretion rate for a $\sim 1.0 M_{\odot}$ WD accretor is $\dot{M}_{\text{Edd}} \simeq 4 \times 10^{-6} M_{\odot} \text{ yr}^{-1}$. The accumulated phase of Case BB (helium shell burning) mass transfer lasts for about 16 000 yr. Assuming the accretion onto the WD to be limited to the Eddington rate, it accretes about $\Delta M_{\text{WD}} = 0.06 M_{\odot}$, which is more than sufficient to spin it up to a high spin rate, as we demonstrate below.

WD accretion and spin up The mass transferred from the helium-star donor carries angular momentum which eventually spins up the WD. Besides material stress, the accretion torque, N acting on the WD has a contribution from both magnetic stress and viscous stress and its effect can be expressed as: $N = \dot{J}_* \equiv (d/dt)(I\Omega_*)$, where J_* is the WD spin angular momentum, Ω_* is its angular velocity and $I = k^2 M_{\text{WD}} R_{\text{WD}}^2 \approx 0.9 \times 10^{50} \text{ g cm}^2$ is its moment of inertia (computed from eqn. (4) of (52)), where k is the gyration radius.

The exchange of angular momentum ($\vec{J}_* = \vec{r} \times \vec{p}$, where \vec{r} is the position vector of a particle, and \vec{p} is its momentum vector) at the magnetospheric boundary eventually leads to a gain of WD spin angular momentum which can approximately be expressed as:

$$\Delta J_* = \int n(\omega, t) \dot{M}_{\text{WD}}(t) \sqrt{GM_{\text{WD}}(t)r_{\text{mag}}(t)} \xi(t) dt \simeq \sqrt{GM_{\text{WD}}r_{\text{mag}}} \Delta M_{\text{WD}} \quad (\text{S12})$$

where M_{WD} denotes the WD mass, \dot{M}_{WD} is its mass-accretion rate, $n(\omega)$ is a dimensionless torque and $\xi \simeq 1$ is a numerical factor which depends on the flow pattern (58, 61, 62). The total amount of mass accreted by the WD is given by ΔM_{WD} , and r_{mag} is the location of the magnetosphere (the Alfvén radius, or the length of the lever arm) defined as the location where the magnetic energy density will begin to control the flow of the material (i.e. where the incoming material couples to the magnetic field lines and co-rotate with the WD magnetosphere), given by (63):

$$r_{\text{mag}} \simeq \left(\frac{B^2 R_{\text{WD}}^6}{\dot{M}_{\text{WD}} \sqrt{2GM_{\text{WD}}}} \right)^{2/7}. \quad (\text{S13})$$

A typical value for the magnetospheric radius of an Eddington-accreting WD (assuming $\dot{M}_{\text{Edd}} = 4 \times 10^{-6} M_{\odot} \text{ yr}^{-1}$) is thus $r_{\text{mag}} \simeq 1 - 16 R_{\text{WD}}$ for a surface magnetic flux density of $B = 10^6 - 10^8 \text{ G}$. For a weaker B-field, the magnetosphere is pushed down to the surface of the WD and the lever arm of the accretion torque is simply R_{WD} .

We can now estimate the minimum spin period, $P_{\text{WD}}^{\text{min}}$ of the WD in the PSR J1141–6545

system for the most favorable torque transmission (see Eq. S12):

$$P_{\text{WD}}^{\min} = \frac{2\pi I}{\sqrt{GM_{\text{WD}}r_{\text{mag}}} \Delta M_{\text{WD}}} \simeq 20 \text{ sec} \left(\frac{R_{\text{WD}}}{r_{\text{mag}}} \right)^{1/2} \quad (\text{S14})$$

where we have inserted our estimate of accreted material of $\Delta M_{\text{WD}} \simeq 0.06 M_{\odot}$.

So far, we have disregarded the possibility of propeller effects at work in case $r_{\text{mag}} > r_{\text{co}}$, where the co-rotation radius is given by:

$$r_{\text{co}} \equiv \left(\frac{GM_{\text{WD}}P_{\text{WD}}^2}{4\pi^2} \right)^{1/3} \simeq 6 R_{\text{WD}} \left(\frac{P_{\text{WD}}}{100 \text{ s}} \right)^{2/3} \quad (\text{S15})$$

for the WD companion to PSR J1141–6545. Hence, we conclude that propeller effects can be disregarded, unless the B-field of the WD is exceptionally strong while its spin period, P_{WD} is very small.

With our derived 99% upper limits on P_{WD}^{\min} being ~ 900 seconds (Figure 2 and S2), we conclude that our interpretation of the PSR J1141–6545 system is consistent with expectations from binary stellar evolution and standard accretion physics. Hence, we use the posterior distribution of the spin-misalignment angle δ_c from the subsequent supernova simulations to further constrain the WD spin to < 200 seconds.

Simulations of the supernova producing PSR J1141–6545 We have examined the the kinematic effects of 70 million simulated supernova (SN) explosions to reproduce the measured orbital parameters of the PSR J1141–6545 system, following the method applied in (60). In our Monte Carlo simulations, we take advantage of our derived masses for the NS ($1.27 M_{\odot}$) and the WD ($1.02 M_{\odot}$) from observations, as well as the measured values of orbital period (here denoted $P_b = 0.198$ days) and eccentricity ($e = 0.172$). Given that PSR J1141–6545 is a young radio pulsar, we neglect any orbital evolution of the system since its formation. We simulate SNe over a 5-dimensional phase space whose parameters are: the pre-SN orbital period, $P_{b,0}$; the final mass of the (ultra-stripped) exploding helium star, M_{He} ; the magnitude of the kick

velocity imparted on the newborn NS, w ; and the two angles defining the direction of the kick velocity, θ and ϕ . We assumed a flat non-informative prior distributions for all these parameters except for θ where a random (isotropic) kick direction leads to a prior distribution of $\sin(\theta)$. The extents of the prior probability distributions are given in Table S1.

Using Monte Carlo methods, we repeatedly select a set of values of $P_{b,0}$, M_{He} , w , θ and ϕ , and solve in each trial for the post-SN orbital parameters as outlined in (60). From the outcome of the initial simulations, we can compare with the values of the PSR J1141–6545 system and iterate by adjusting the pre-SN parameter space until the outcome matches with the observed post-SN values within a chosen error margin of 3%. In Figure S11, we show the results of our simulations. The chosen solutions are centered on the observed values of (P_b, e) with the accepted error margin of $\pm 3\%$ in both P_b and e as shown in Figure S11A. Figure S11B shows the post-SN distribution of 3D systemic velocities. Figure S11C and D show the pre-SN orbital period, $P_{b,0}$ and the mass of the exploding star, M_{He} . Panel E shows the applied kick magnitudes for all successful solutions; and Figure S11F shows the distribution of resulting post-SN misalignment angles of the WD.

In these simulations, we restricted the mass of the exploding star to $\leq 1.7 M_\odot$ based on the mass-transfer calculations (see above), which resulted in an ultra-stripped star prior to the explosion. Given that the NS mass of PSR J1141–6545 is rather low ($1.27 M_\odot$), we also restricted the kick magnitude to $\leq 400 \text{ km s}^{-1}$ — an upper limit derived for the similar second SN explosion in ultra-stripped SNe producing double NS systems (60). The latter constraint is also supported by the possible correlation between NS mass and kick magnitude (60, 64).

The misalignment angle of the WD is found to be less than 50° at the 99% confidence level. Misalignment angles in the interval between $40^\circ - 90^\circ$ appear in 10% of the cases only if we allow for extremely large kicks ($400 - 1000 \text{ km s}^{-1}$), and masses of the exploding star up to $2.5 - 3.0 M_\odot$ (which are disfavoured by the evolution and expansion of the progenitor helium

star in binary stellar evolution models).

From additional simulations, we also find that the distribution of resulting misalignment angles is insensitive to changes in the allowed error margin in post-SN orbital period and eccentricity (e.g. applying $\pm 10\%$ yields a very similar result). This is because post-SN systems with properties somewhat similar to those of PSR J1141–6545, would all have fairly small SN ejecta and a small NS mass, resulting in a relatively small kick, and thus small misalignment angles.

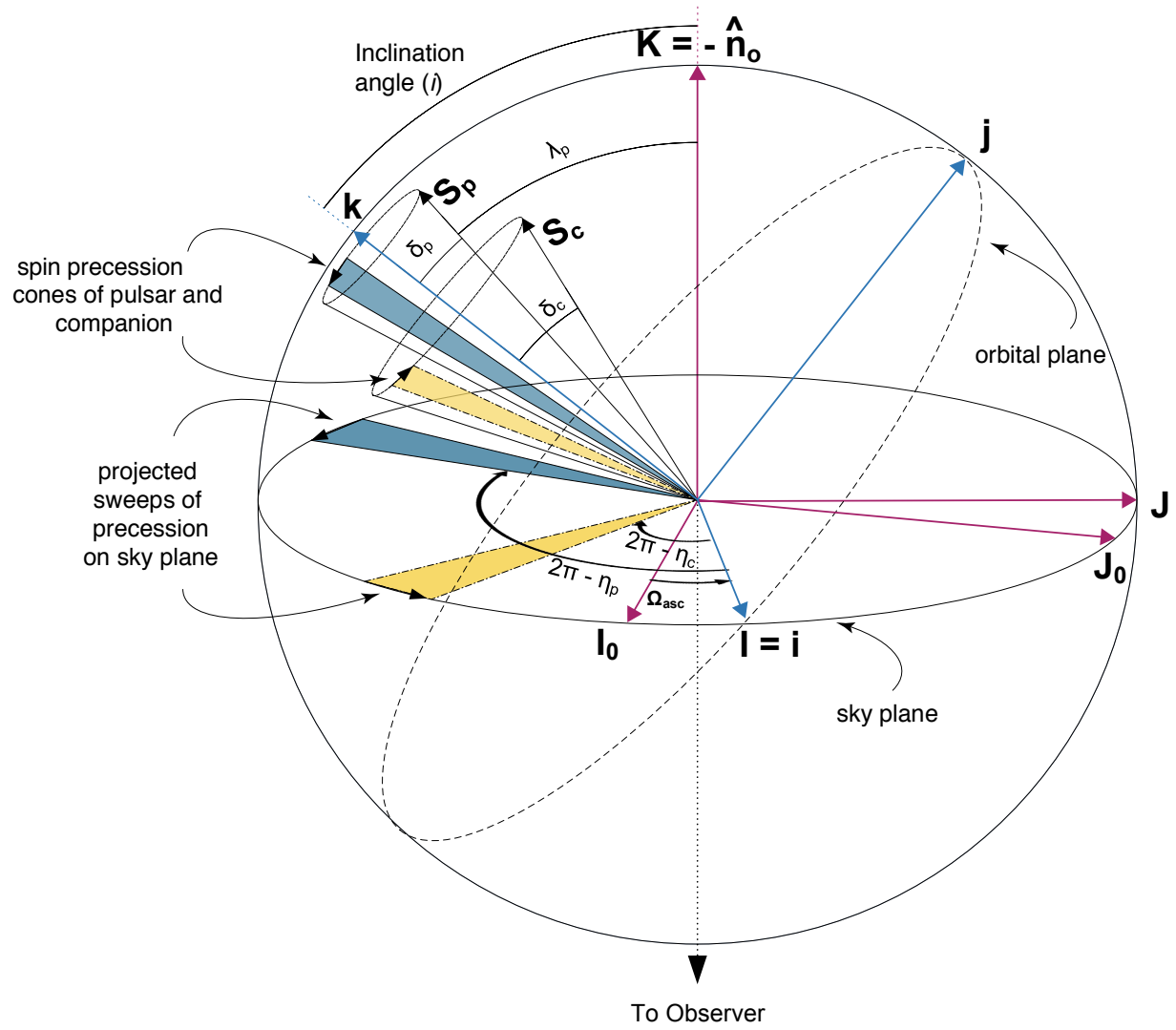


Figure S1. Definition of spin and orbital geometry. Illustration of various angles in the spin and orbital geometry of the system, using the "DT92" definitions (10). The unit vectors \mathbf{I}_0 and \mathbf{J}_0 denote the plane of the sky, with \mathbf{K} denoting the line of sight from the observer to

the pulsar, and perpendicular to the sky plane. The unit vectors $\mathbf{I} \equiv \mathbf{i}$ and \mathbf{j} form the orbital plane, inclined at an angle i to the sky plane and rotated in azimuth by Ω_{asc} . The normal to the orbital plane (\mathbf{k}) is then by definition the direction of the orbital angular momentum vector \mathbf{L} which is approximated here to be also the direction of the total angular momentum vector \mathbf{L}_{tot} , given that the magnitude of the angular momenta of the component stars are much smaller than $|\mathbf{L}|$ (See Figure 1 for the case where this approximation is not made). The spin angular momentum vectors of the pulsar and the companion are given by \mathbf{S}_p and \mathbf{S}_c respectively, which are misaligned from \mathbf{L}_{tot} by angles δ_p and δ_c . λ_p is defined as the angle between \mathbf{S}_p and \mathbf{K} . Spin precession causes the spin vectors (\mathbf{S}_p , \mathbf{S}_c) to precess around \mathbf{L}_{tot} at a rate denoted by Ω_p^{geod} and Ω_c^{geod} respectively. This causes the instantaneous precession phases of the pulsar and the companion to evolve in time, thereby sweeping out “precession cones”. These precessional sweeps projected onto the sky plane sweep the corresponding longitudes of precession (η_p, η_c) , as shown by the blue and yellow shaded sweeps on the precession cones and the sky plane. These angles are measured from \mathbf{I} and the complementary angles $(2\pi - \eta_p)$ and $(2\pi - \eta_c)$ are shown for clarity.

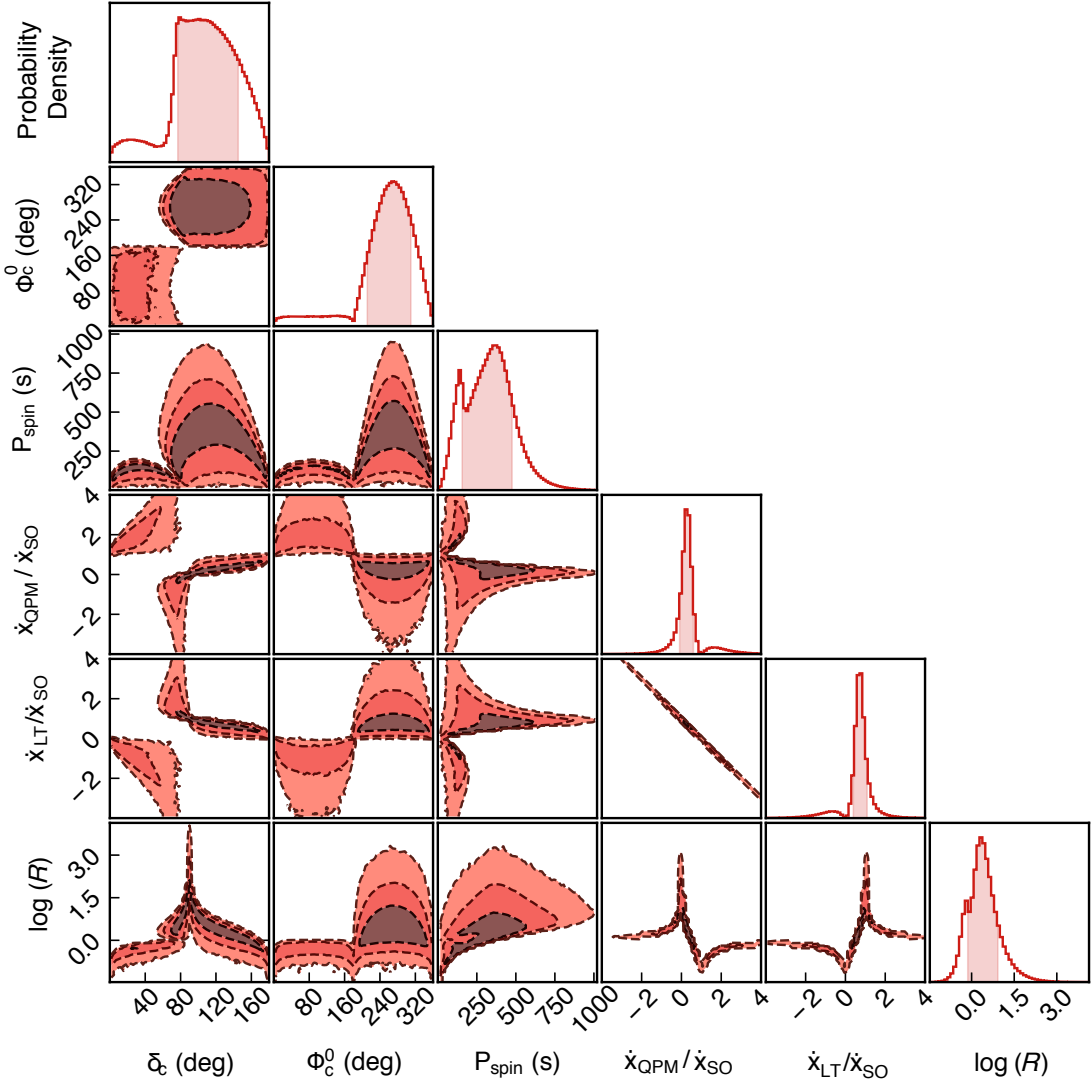


Figure S2. Contributions to orbital precession from WD rotation. This correlation plot shows the fractional contribution to \dot{x}_{SO} from \dot{x}_{QPM} and \dot{x}_{LT} and their absolute ratio (R) as a function of the apriori unknown angles $\{\delta_c, \Phi_c^0\}$ and P_{WD} . The off-diagonal panels are 2D probability densities with dashed contours enclosing 68%, 95% and 99% iso-likelihood confidence intervals, shaded in progressively darker colors. The diagonal probability densities with solid lines are marginalised posterior probability distributions of the corresponding dimensions, with shaded regions indicating the 68% iso-likelihood contours.

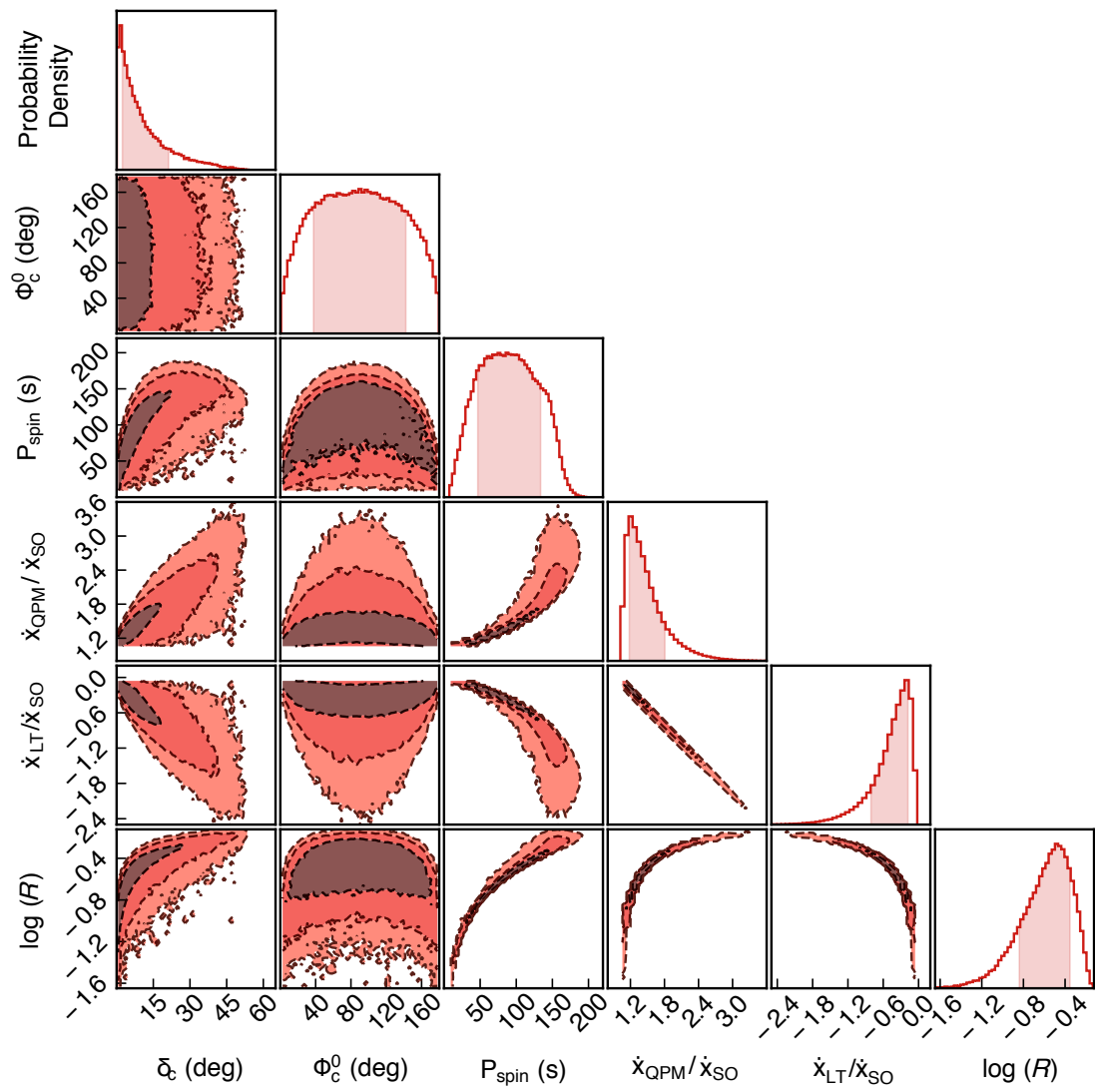


Figure S3. Contributions to orbital precession from WD rotation constrained by binary evolution simulations. Same as Figure S2, but now with a constrained prior on δ_c given by the binary evolution simulations (see text).

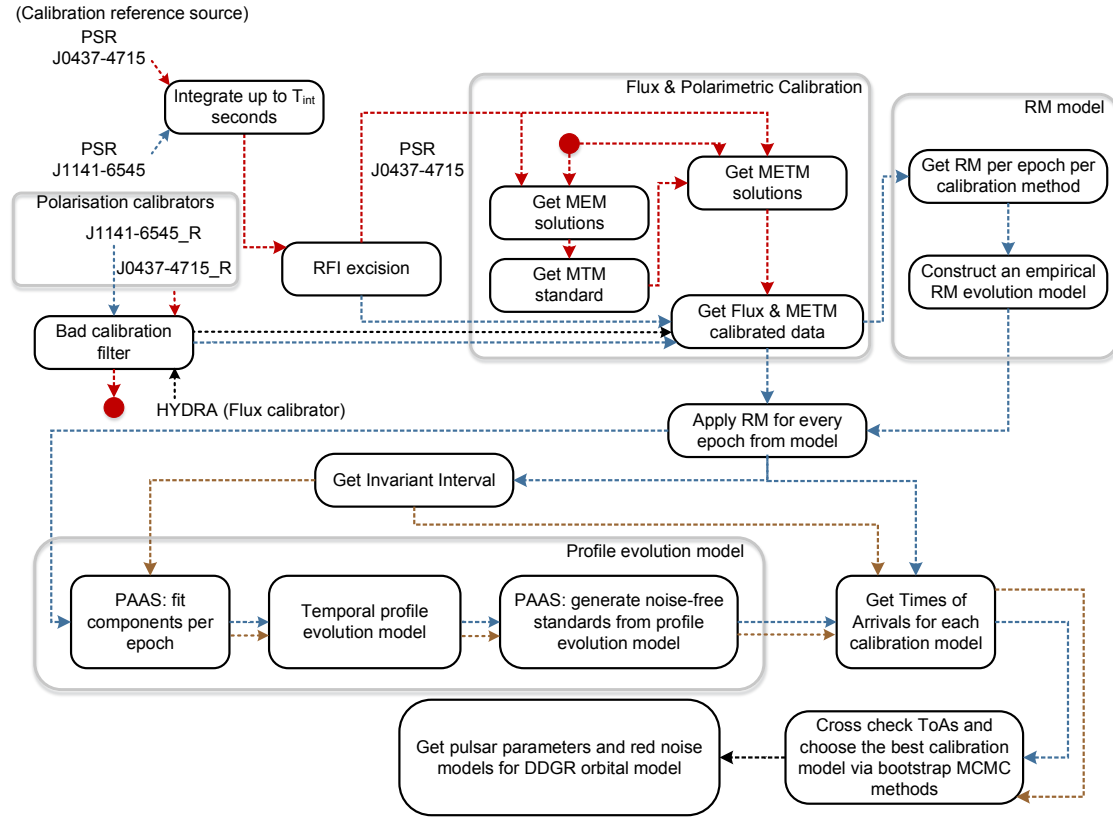


Figure S4. Reduction process for Parkes data. A block diagram of the data reduction process for the Parkes 20cm multi-beam receiver data.

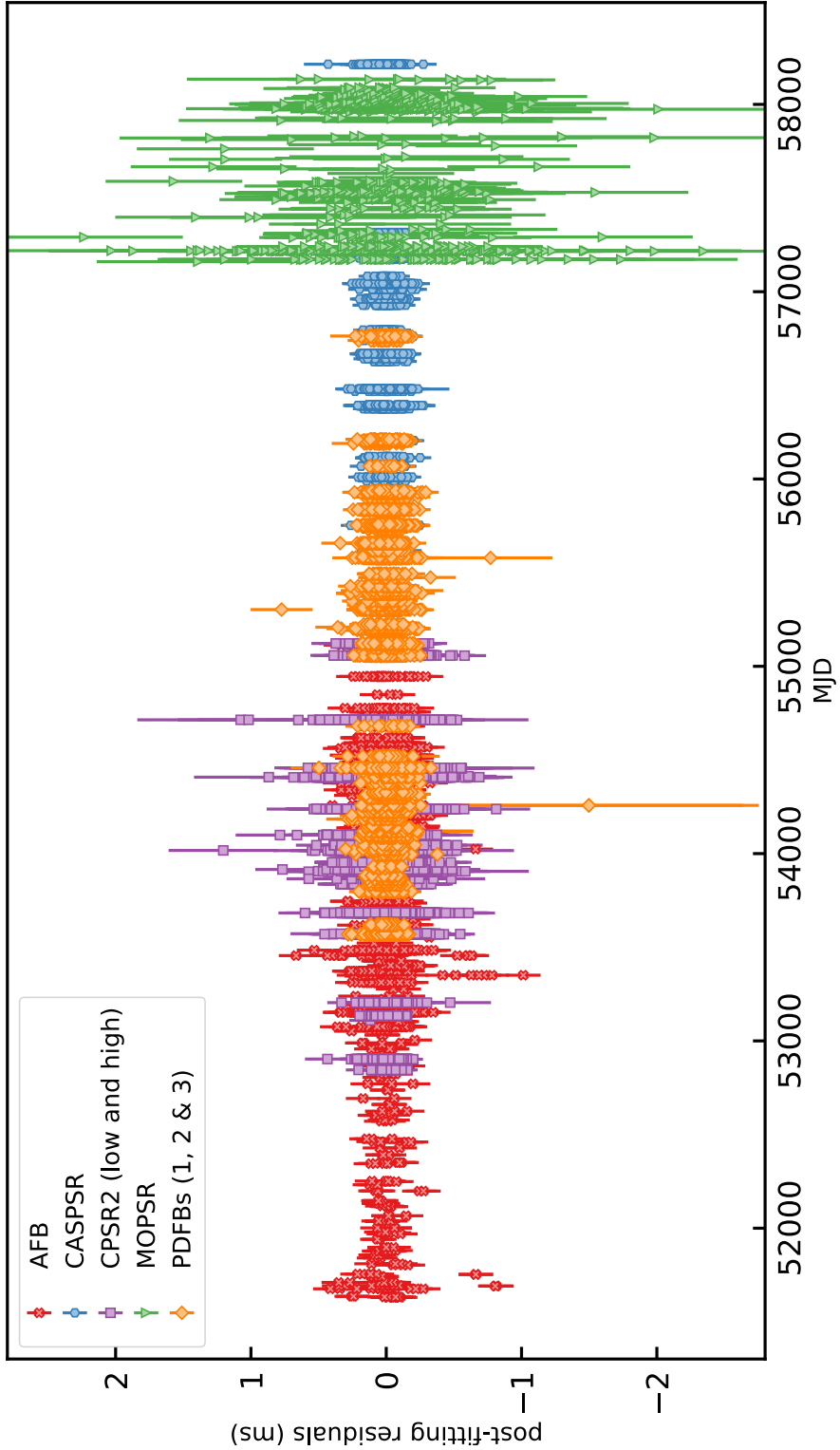


Figure S5. Timing residuals. A plot of the residual errors in the arrival times of ~ 22000 ToAs recorded over the course of our dataset. The different colors and symbols represent different backends (see text for details). The residual timing precision of the pulsar is $\sim 95.6 \mu s$

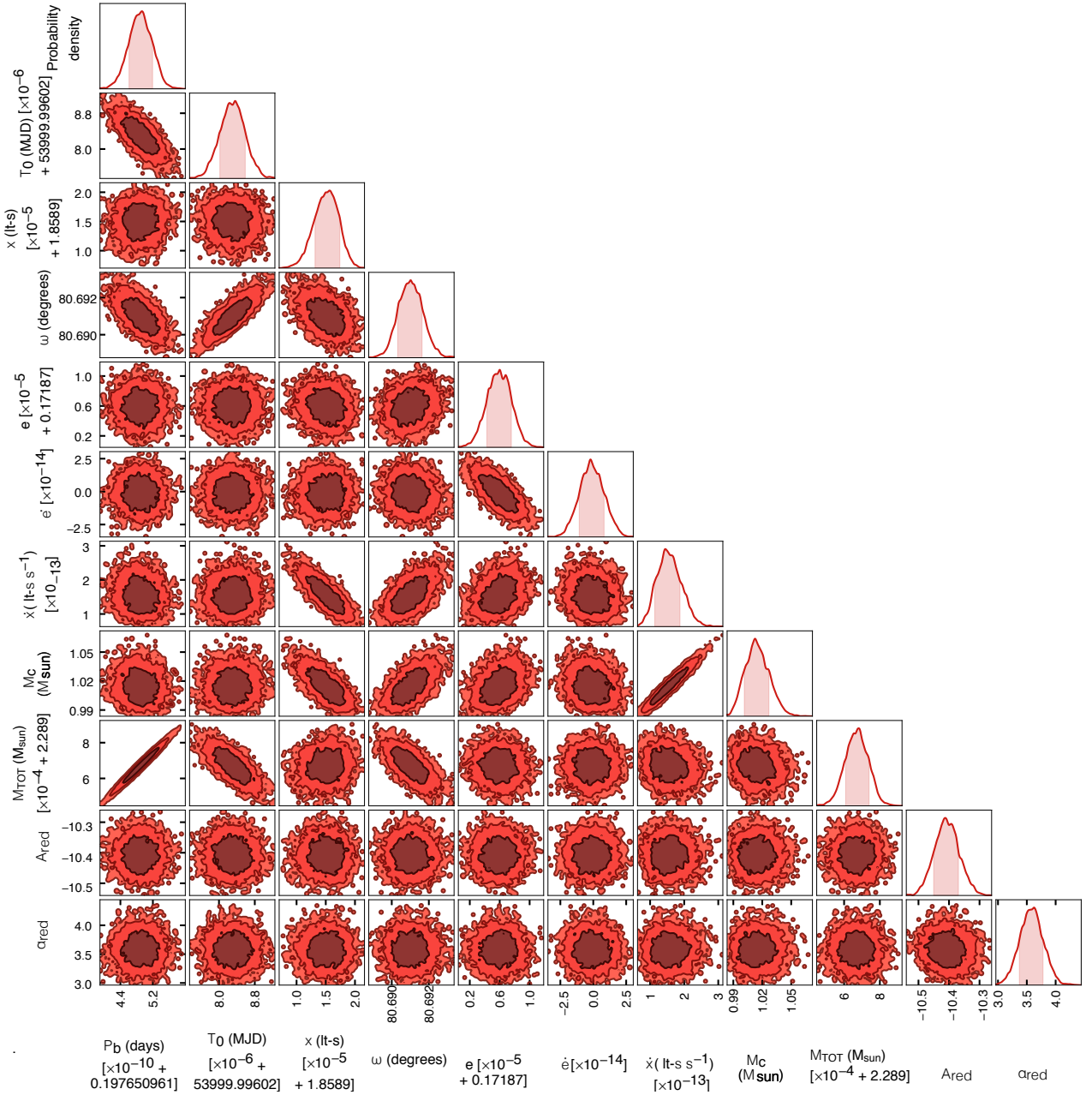


Figure S6. Correlations between orbital parameters. An overview of the posterior distributions of the pulsar's DDGR orbital parameters and the red-noise model, showing the correlation between different parameters.

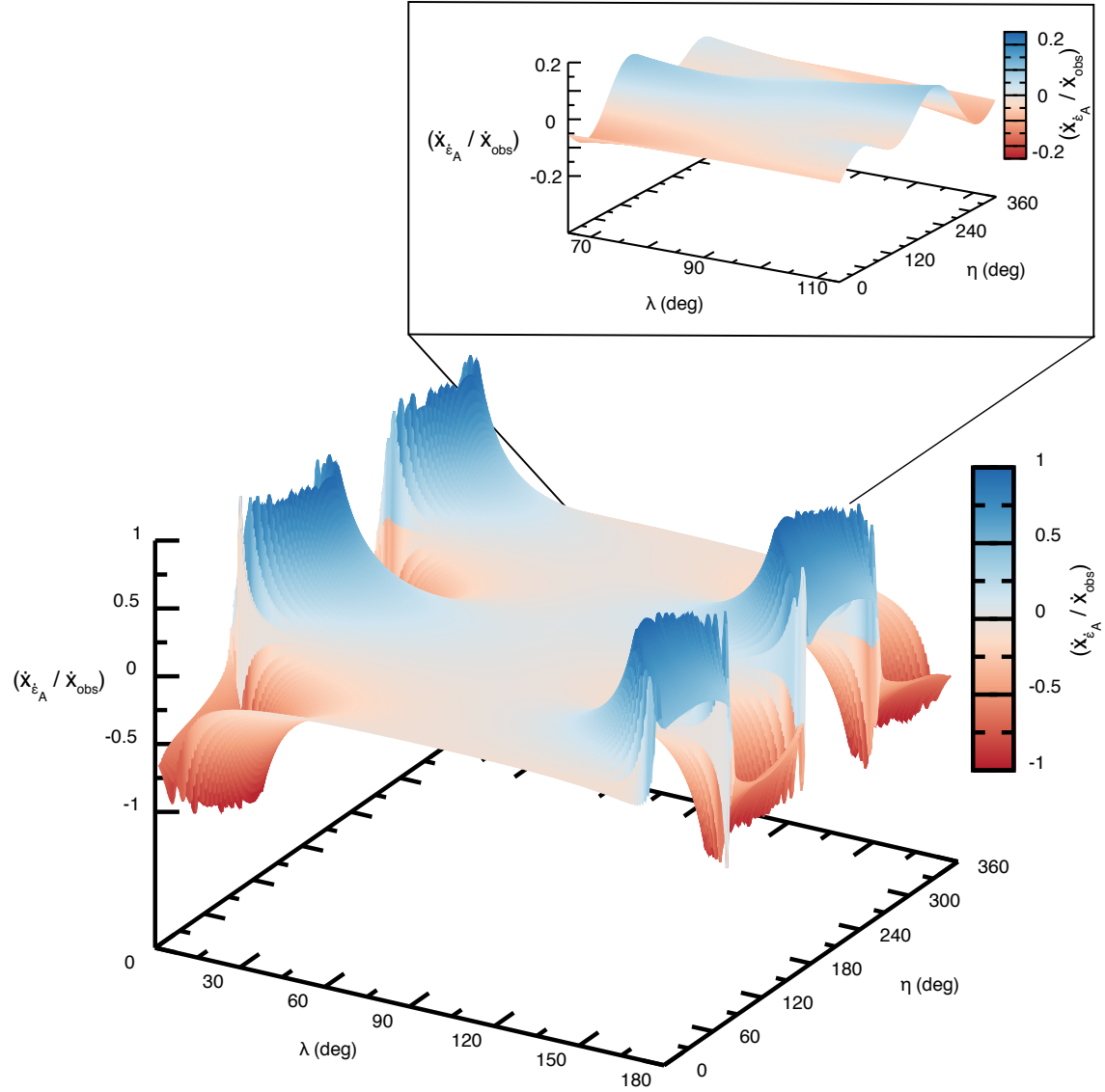


Figure S7. Contribution to \dot{x}_{obs} due to changing aberration. The fractional contribution to \dot{x}_{obs} from the rate of change of aberration as a function of the initial polar angles (λ_p, η_p) of the pulsar. As $\lambda_p \rightarrow 0^\circ$ (or 180°), $\dot{x}_{e_A}/\dot{x}_{\text{obs}} \rightarrow \pm\infty$ depending on η_p . The vertical range is limited to $-1 < \dot{x}_{e_A}/\dot{x}_{\text{obs}} < 1$ for clarity. The inset shows the range of λ_p estimated from analysis of the temporal evolution of the observed pulse profile (19). With this constraint, it can be seen that the maximum contribution from the rate of change of aberration is only $\sim 20\%$ of \dot{x}_{obs} .

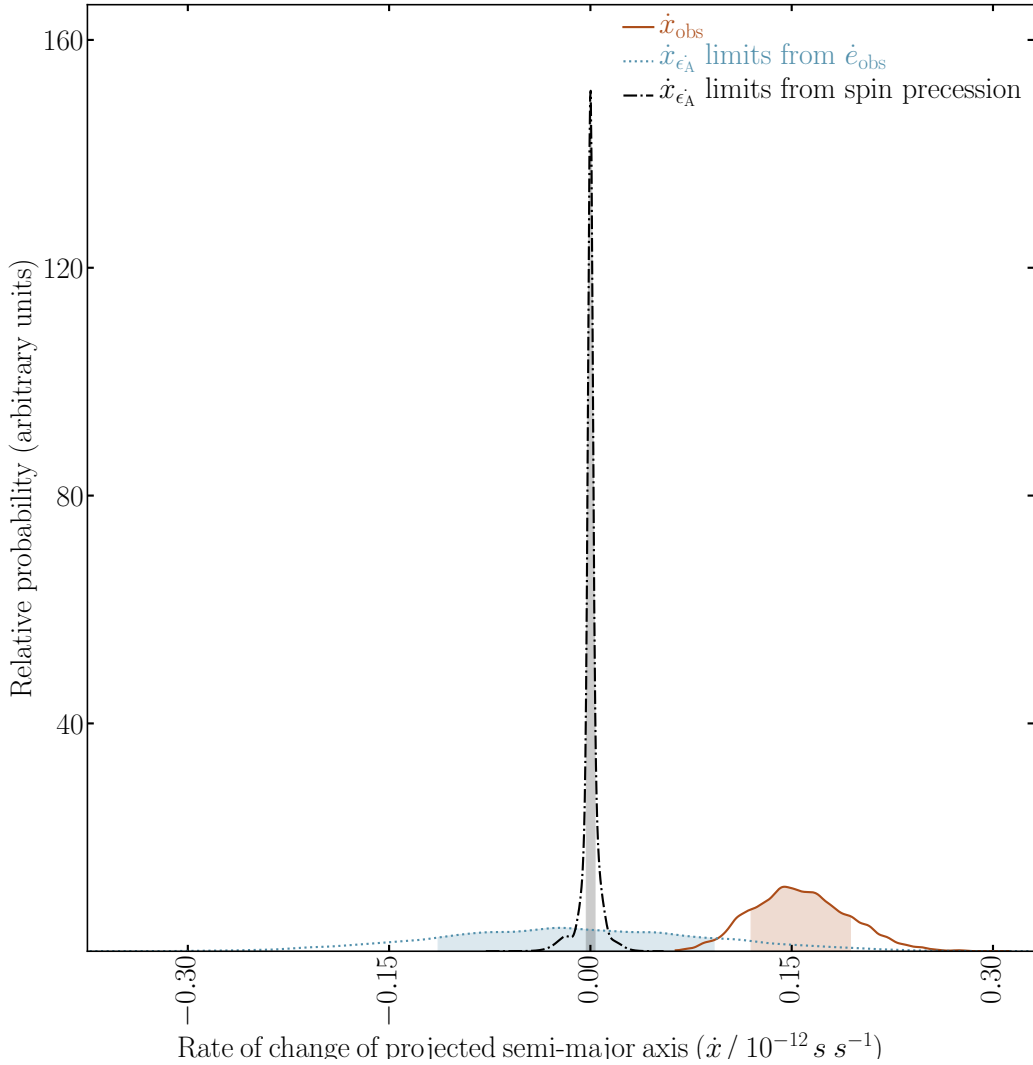


Figure S8. Limits on orbital precession due to changing aberration. Limits on the contributions to the observed rate of change of the projected semi-major axis (\dot{x}_{obs}) due to the rate of change of aberration of the pulse profile (\dot{x}_{ϵ_A}). The limit in light blue comes from our non-detection of a change in eccentricity (\dot{e}). The more stringent limit in gray, comes from modelling the pulsar's profile evolution due to relativistic spin precession (19). The observed value, \dot{x}_{obs} , is plotted in red. The shaded regions denote the 68% confidence intervals.

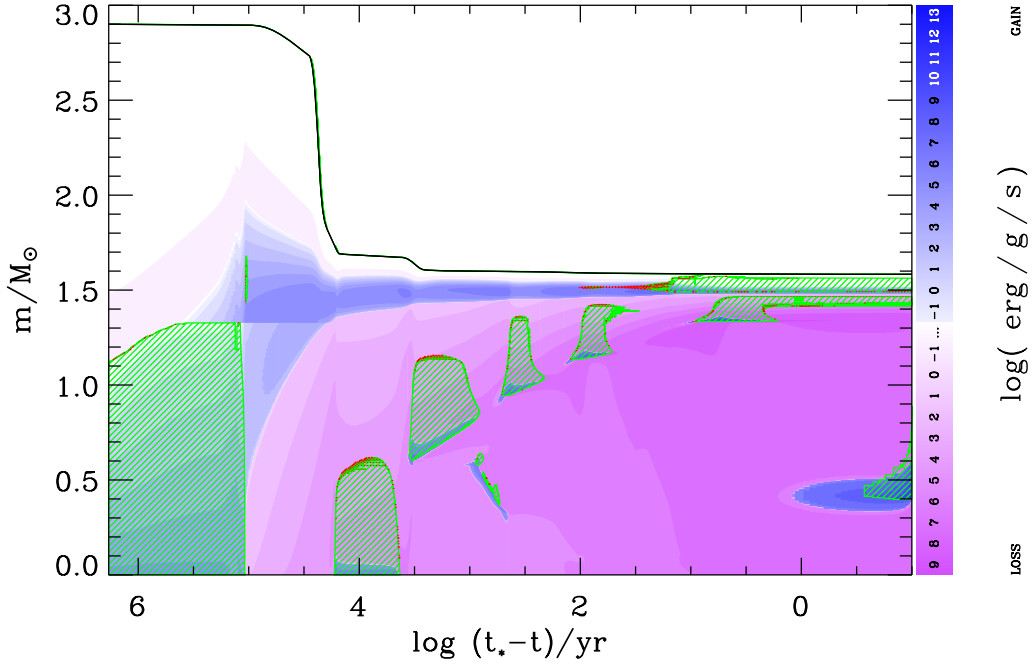


Figure S9. Kippenhahn diagram of a $2.9 M_{\odot}$ helium star undergoing Case BB RLO to a WD accretor. Cross-sections of the helium star are shown in mass-coordinates (m/M_{\odot}) from the centre to the surface of the star, as a function of stellar age. The value $(t_* - t)/\text{yr}$ is the remaining time of our calculations, spanning a total time of $t_* \simeq 1.8$ Myr. The green hatched areas denote zones with convection. The intensity of the blue/purple regions indicates the net energy-production rate. We expect the star to undergo an iron-core collapse about 10 yr after the off-center oxygen ignition (at $m/M_{\odot} \simeq 0.4$, when $\log(t_* - t) = 0.0$).

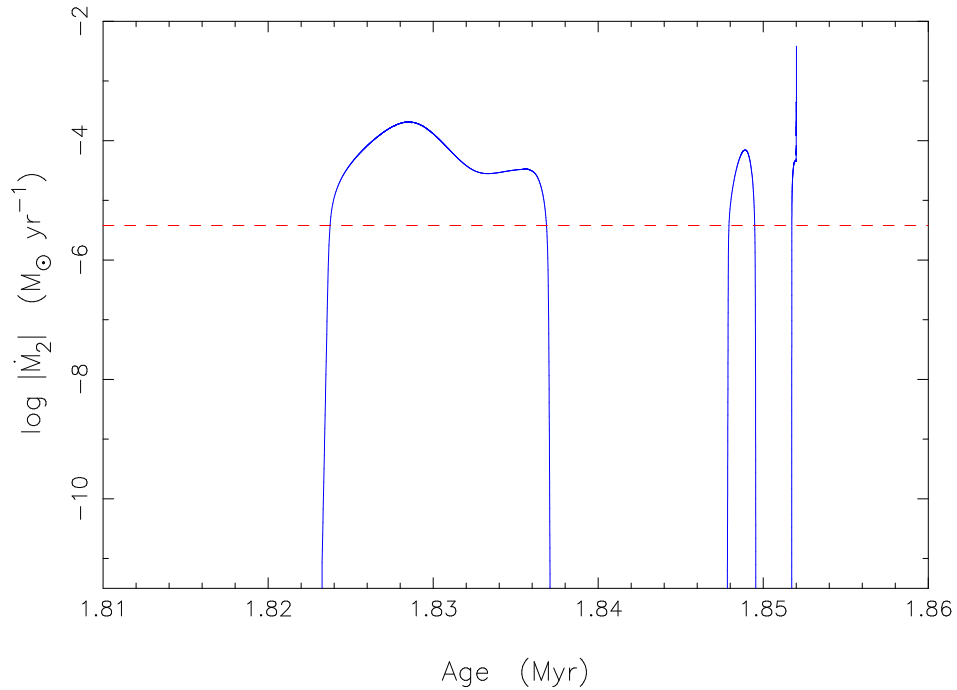


Figure S10. Mass-transfer rate ($|\dot{M}_2|$) as a function of stellar age for the helium-star evolution plotted in Figure S9. During RLO, the mass-transfer rate exceeds the Eddington rate, by more than an order of magnitude, marked by the horizontal red dashed line at $|\dot{M}_2| = \dot{M}_{\text{Edd}} = 4 \times 10^{-6} M_{\odot} \text{yr}^{-1}$ for the WD accretor.

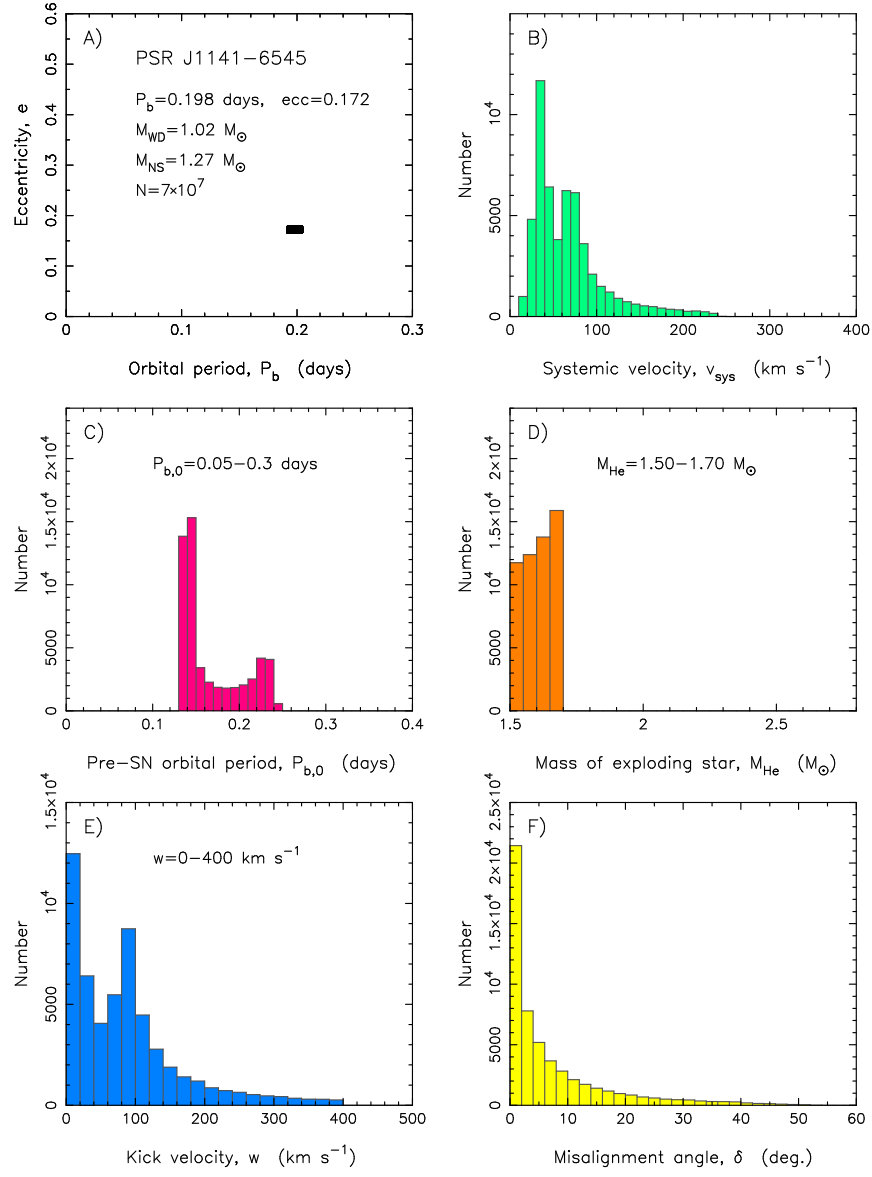


Figure S11. Supernova explosion simulations. Properties and constraints on the formation of the PSR J1141–6545 system based on Monte Carlo simulations of 70 million SN explosions following the method of (60). The six panels display distributions of (A–F): post-SN orbital period and eccentricity, post-SN 3D systemic velocity, pre-SN orbital period, pre-SN mass of exploding helium star, magnitude of SN kick velocity, and misalignment angle of the WD.

Table S1. Prior distributions for SN simulations. To obtain the initial binary parameters that will produce systems that resemble PSR J1141–6545, the following SN prior distributions of parameters were used.

| Model parameter | Type of prior | Bounds |
|-------------------|---------------|------------------------------|
| $P_{\text{b},0}$ | Uniform | by iteration - see text |
| M_{He} | Uniform | $[1.5, 1.7] M_{\odot}$ |
| w_{kick} | Uniform | $[0, 400] \text{ km s}^{-1}$ |
| θ | $\sin \theta$ | $[0, \pi]$ |
| ϕ | Uniform | $[0, 2\pi]$ |

References and Notes

1. I. Ciufolini, J. A. Wheeler, *Gravitation and Inertia* (Princeton Univ. Press, 1995).
2. J. Lense, H. Thirring, *Phys. Z.* **19**, 156 (1918).
3. I. Ciufolini, E. C. Pavlis, A confirmation of the general relativistic prediction of the Lense–Thirring effect. *Nature* **431**, 958–960 (2004). [doi:10.1038/nature03007](https://doi.org/10.1038/nature03007) [Medline](#)
4. C. W. F. Everitt, D. B. DeBra, B. W. Parkinson, J. P. Turneaure, J. W. Conklin, M. I. Heifetz, G. M. Keiser, A. S. Silbergleit, T. Holmes, J. Kolodziejczak, M. Al-Meshari, J. C. Mester, B. Muhlfelder, V. G. Solomonik, K. Stahl, P. W. Worden Jr., W. Bencze, S. Buchman, B. Clarke, A. Al-Jadaan, H. Al-Jibreel, J. Li, J. A. Lipa, J. M. Lockhart, B. Al-Suwaidan, M. Taber, S. Wang, Gravity Probe B: Final results of a space experiment to test general relativity. *Phys. Rev. Lett.* **106**, 221101 (2011).
[doi:10.1103/PhysRevLett.106.221101](https://doi.org/10.1103/PhysRevLett.106.221101) [Medline](#)
5. C. S. Reynolds, Observing black holes spin. *New Astron.* **3**, 41–47 (2019).
[doi:10.1038/s41550-018-0665-z](https://doi.org/10.1038/s41550-018-0665-z)
6. N. Wex, The second post-Newtonian motion of compact binary-star systems with spin. *Class. Quantum Gravity* **12**, 983–1005 (1995). [doi:10.1088/0264-9381/12/4/009](https://doi.org/10.1088/0264-9381/12/4/009)
7. V. M. Kaspi, M. Bailes, R. N. Manchester, B. W. Stappers, J. F. Bell, Evidence from a processing pulsar orbit for a neutron-star birth kick. *Nature* **381**, 584–586 (1996).
[doi:10.1038/381584a0](https://doi.org/10.1038/381584a0)
8. Materials and methods are available as supplementary materials.
9. D. R. Lorimer, M. Kramer, *Handbook of Pulsar Astronomy* (Cambridge Univ. Press, 2012).
10. T. Damour, J. H. Taylor, Strong-field tests of relativistic gravity and binary pulsars. *Phys. Rev. D Part. Fields* **45**, 1840–1868 (1992). [doi:10.1103/PhysRevD.45.1840](https://doi.org/10.1103/PhysRevD.45.1840) [Medline](#)
11. T. Damour, N. Deruelle, General relativistic celestial mechanics of binary systems. I. The post-Newtonian motion. *Ann. Inst. Henri Poincaré Phys. Théor.* **43**, 107–132 (1985).
12. T. Damour, N. Deruelle, General relativistic celestial mechanics of binary systems. II. The post-Newtonian timing formula. *Ann. Inst. Henri Poincaré Phys. Théor.* **44**, 263–292 (1986).
13. V. M. Kaspi, A. G. Lyne, R. N. Manchester, F. Crawford, F. Camilo, J. F. Bell, N. D’Amico, I. H. Stairs, N. P. F. McKay, D. J. Morris, A. Possenti, Discovery of a Young Radio Pulsar in a Relativistic Binary Orbit. *Astrophys. J.* **543**, 321–327 (2000).
[doi:10.1086/317103](https://doi.org/10.1086/317103)
14. J. Antoniadis, C. G. Bassa, N. Wex, M. Kramer, R. Napiwotzki, A white dwarf companion to the relativistic pulsar PSR J1141–6545. *Mon. Not. R. Astron. Soc.* **412**, 580–584 (2011).
[doi:10.1111/j.1365-2966.2010.17929.x](https://doi.org/10.1111/j.1365-2966.2010.17929.x)
15. T. M. Tauris, T. Sennels, *Astron. Astrophys.* **355**, 236 (2000).
16. R. P. Church, S. J. Bush, C. A. Tout, M. B. Davies, Detailed models of the binary pulsars J1141–6545 and B2303+46. *Mon. Not. R. Astron. Soc.* **372**, 715–727 (2006).
[doi:10.1111/j.1365-2966.2006.10897.x](https://doi.org/10.1111/j.1365-2966.2006.10897.x)

17. B. M. Barker, R. F. O'Connell, Gravitational two-body problem with arbitrary masses, spins, and quadrupole moments. *Phys. Rev. D Part. Fields* **12**, 329–335 (1975). [doi:10.1103/PhysRevD.12.329](https://doi.org/10.1103/PhysRevD.12.329)
18. A. W. Hotan, W. van Straten, R. N. Manchester, PSRCHIVE and PSRFITS: An open approach to radio pulsar data storage and analysis. *Astron. Soc. Aust.* **21**, 302–309 (2004). [doi:10.1071/AS04022](https://doi.org/10.1071/AS04022)
19. V. Venkatraman Krishnan, M. Bailes, W. van Straten, E. F. Keane, M. Kramer, N. D. R. Bhat, C. Flynn, S. Osłowski, Relativistic spin precession in the binary PSR J1141–6545. *Astrophys. J.* **873**, L15 (2019). [doi:10.3847/2041-8213/ab0a03](https://doi.org/10.3847/2041-8213/ab0a03)
20. M. Bailes, A. Jameson, C. Flynn, T. Bateman, E. D. Barr, S. Bhandari, J. D. Bunton, M. Caleb, D. Campbell-Wilson, W. Farah, B. Gaensler, A. J. Green, R. W. Hunstead, F. Jankowski, E. F. Keane, V. V. Krishnan, T. Murphy, M. O'Neill, S. Osłowski, A. Parthasarathy, V. Ravi, P. Rosado, D. Temby, The UTMOST: A Hybrid Digital Signal Processor Transforms the Molonglo Observatory Synthesis Telescope. *Astron. Soc. Aust.* **34**, e045 (2017). [doi:10.1017/pasa.2017.39](https://doi.org/10.1017/pasa.2017.39)
21. J. H. Taylor, J. M. Weisberg, Further experimental tests of relativistic gravity using the binary pulsar PSR 1913+16. *Astrophys. J.* **345**, 434 (1989). [doi:10.1086/167917](https://doi.org/10.1086/167917)
22. M. S. Kehl, N. Wex, M. Kramer, K. Liu, in *Fourteenth Marcel Grossmann Meeting—MG14* (2018), pp. 1860–1865.
23. S. D. Kawaler, in *19th European Workshop on White Dwarfs*, P. Dufour, P. Bergeron, G. Fontaine, eds. (2015), vol. 493 of *Astronomical Society of the Pacific Conference Series*, p. 65.
24. J. J. Hermes, S. D. Kawaler, A. D. Romero, S. O. Kepler, P.-E. Tremblay, K. J. Bell, B. H. Dunlap, M. H. Montgomery, B. T. Gänsicke, J. C. Clemens, E. Dennihy, S. Redfield, Evidence from *K2* for Rapid Rotation in the Descendant of an Intermediate-mass Star. *Astrophys. J.* **841**, L2 (2017). [doi:10.3847/2041-8213/aa6ffc](https://doi.org/10.3847/2041-8213/aa6ffc)
25. T. M. Tauris, N. Langer, T. J. Moriya, P. Podsiadlowski, S.-C. Yoon, S. I. Blinnikov, Ultra-stripped type Ic supernovae from close binary evolution. *Astrophys. J.* **778**, L23 (2013). [doi:10.1088/2041-8205/778/2/L23](https://doi.org/10.1088/2041-8205/778/2/L23)
26. T. M. Tauris, N. Langer, P. Podsiadlowski, Ultra-stripped supernovae: Progenitors and fate. *Mon. Not. R. Astron. Soc.* **451**, 2123–2144 (2015). [doi:10.1093/mnras/stv990](https://doi.org/10.1093/mnras/stv990)
27. K. De, M. M. Kasliwal, E. O. Ofek, T. J. Moriya, J. Burke, Y. Cao, S. B. Cenko, G. B. Doran, G. E. Duggan, R. P. Fender, C. Fransson, A. Gal-Yam, A. Horesh, S. R. Kulkarni, R. R. Laher, R. Lunnan, I. Manulis, F. Masci, P. A. Mazzali, P. E. Nugent, D. A. Perley, T. Petrushevska, A. L. Piro, C. Rumsey, J. Sollerman, M. Sullivan, F. Taddia, A hot and fast ultra-stripped supernova that likely formed a compact neutron star binary. *Science* **362**, 201–206 (2018). [doi:10.1126/science.aas8693](https://doi.org/10.1126/science.aas8693) [Medline](#)
28. V. Venkatraman Krishnan, M. Bailes, W. van Straten, N. Wex, P. C. C. Freire, E. F. Keane, T. M. Tauris, P. A. Rosado, N. D. R. Bhat, C. Flynn, A. Jameson, S. Osłowski, Data and software release for: Lense–Thirring frame dragging induced by a fast-rotating white dwarf in a binary pulsar system, Zenodo (2019); <https://doi.org/10.5281/zenodo.3555380>.

29. L. Staveley-Smith, W. E. Wilson, T. S. Bird, M. J. Disney, R. D. Ekers, K. C. Freeman, R. F. Haynes, M. W. Sinclair, R. A. Vaile, R. L. Webster, A. E. Wright, The Parkes 21 cm Multibeam Receiver. *Astron. Soc. Aust.* **13**, 243–248 (1996). [doi:10.1017/S1323358000020919](https://doi.org/10.1017/S1323358000020919)
30. R. N. Manchester, G. Hobbs, M. Bailes, W. A. Coles, W. van Straten, M. J. Keith, R. M. Shannon, N. D. R. Bhat, A. Brown, S. G. Burke-Spolaor, D. J. Champion, A. Chaudhary, R. T. Edwards, G. Hampson, A. W. Hotan, A. Jameson, F. A. Jenet, M. J. Kesteven, J. Khoo, J. Kocz, K. Maciesiak, S. Osłowski, V. Ravi, J. R. Reynolds, J. M. Sarkissian, J. P. W. Verbiest, Z. L. Wen, W. E. Wilson, D. Yardley, W. M. Yan, X. P. You, The Parkes Pulsar Timing Array Project. *Astron. Soc. Aust.* **30**, e017 (2013). [doi:10.1017/pasa.2012.017](https://doi.org/10.1017/pasa.2012.017)
31. W. van Straten, M. Bailes, DSPSR: Digital Signal Processing Software for Pulsar Astronomy. *Astron. Soc. Aust.* **28**, 1–14 (2011). [doi:10.1071/AS10021](https://doi.org/10.1071/AS10021)
32. R. T. Edwards, G. B. Hobbs, R. N. Manchester, TEMPO2, a new pulsar timing package - II. The timing model and precision estimates. *Mon. Not. R. Astron. Soc.* **372**, 1549–1574 (2006). [doi:10.1111/j.1365-2966.2006.10870.x](https://doi.org/10.1111/j.1365-2966.2006.10870.x)
33. W. van Straten, High-fidelity radio astronomical polarimetry using a millisecond pulsar as a polarized reference source. *Astrophys. J. Suppl. Ser.* **204**, 13 (2013). [doi:10.1088/0067-0049/204/1/13](https://doi.org/10.1088/0067-0049/204/1/13)
34. M. C. Britton, Radio astronomical polarimetry and the Lorentz group. *Astrophys. J.* **532**, 1240–1244 (2000). [doi:10.1086/308595](https://doi.org/10.1086/308595)
35. L. Lentati, P. Alexander, M. P. Hobson, F. Feroz, R. van Haasteren, K. J. Lee, R. M. Shannon, temponest: A Bayesian approach to pulsar timing analysis. *Mon. Not. R. Astron. Soc.* **437**, 3004–3023 (2014). [doi:10.1093/mnras/stt2122](https://doi.org/10.1093/mnras/stt2122)
36. R. N. Manchester, M. Kramer, I. H. Stairs, M. Burgay, F. Camilo, G. B. Hobbs, D. R. Lorimer, A. G. Lyne, M. A. McLaughlin, C. A. McPhee, A. Possenti, J. E. Reynolds, W. van Straten, Observations and modeling of relativistic spin precession in PSR J1141–6545. *Astrophys. J.* **710**, 1694–1709 (2010). [doi:10.1088/0004-637X/710/2/1694](https://doi.org/10.1088/0004-637X/710/2/1694)
37. F. Jankowski, M. Bailes, W. van Straten, E. F. Keane, C. Flynn, E. D. Barr, T. Bateman, S. Bhandari, M. Caleb, D. Campbell-Wilson, W. Farah, A. J. Green, R. W. Hunstead, A. Jameson, S. Osłowski, A. Parthasarathy, P. A. Rosado, V. Venkatraman Krishnan, The UTMOST pulsar timing programme I: Overview and first results. *Mon. Not. R. Astron. Soc.* **484**, 3691–3712 (2019). [doi:10.1093/mnras/sty3390](https://doi.org/10.1093/mnras/sty3390)
38. W. van Straten, Radio astronomical polarimetry and point-source calibration. *Astrophys. J. Suppl. Ser.* **152**, 129–135 (2004). [doi:10.1086/383187](https://doi.org/10.1086/383187)
39. W. van Straten, Radio astronomical polarimetry and high-precision pulsar timing. *Astrophys. J.* **642**, 1004–1011 (2006). [doi:10.1086/501001](https://doi.org/10.1086/501001)
40. F. Feroz, M. P. Hobson, M. Bridges, MultiNest: An efficient and robust Bayesian inference tool for cosmology and particle physics. *Mon. Not. R. Astron. Soc.* **398**, 1601–1614 (2009). [doi:10.1111/j.1365-2966.2009.14548.x](https://doi.org/10.1111/j.1365-2966.2009.14548.x)

41. S. M. Ord, M. Bailes, W. van Straten, The scintillation velocity of the relativistic binary pulsar PSR J1141–6545. *Astrophys. J.* **574**, L75–L78 (2002). [doi:10.1086/342218](https://doi.org/10.1086/342218)
42. D. J. Reardon, W. A. Coles, G. Hobbs, S. Ord, M. Kerr, M. Bailes, N. D. R. Bhat, V. Venkatraman Krishnan, Modelling annual and orbital variations in the scintillation of the relativistic binary PSR J1141–6545. *Mon. Not. R. Astron. Soc.* **485**, 4389–4403 (2019). [doi:10.1093/mnras/stz643](https://doi.org/10.1093/mnras/stz643)
43. J. M. Cordes, T. J. W. Lazio, NE2001.I. A new model for the galactic distribution of free electrons and its fluctuations. [arXiv:astro-ph/0207156](https://arxiv.org/abs/astro-ph/0207156) [astro-ph] (8 July 2002).
44. J. M. Yao, R. N. Manchester, N. Wang, A new electron-density model for estimation of pulsar and FRB distances. *Astrophys. J.* **835**, 29 (2017). [doi:10.3847/1538-4357/835/1/29](https://doi.org/10.3847/1538-4357/835/1/29)
45. S. M. Ord, M. Bailes, W. van Straten, A neutral hydrogen distance limit to the relativistic binary PSR J1141-6545. *Mon. Not. Roy. Astron. Soc.* **337**, 409 (2002).
46. T. Damour, J. H. Taylor, On the orbital period change of the binary pulsar PSR 1913 + 16. *Astrophys. J.* **366**, 501 (1991). [doi:10.1086/169585](https://doi.org/10.1086/169585)
47. T. Damour, G. Esposito-Farese, Tensor-multi-scalar theories of gravitation. *Class. Quantum Gravity* **9**, 2093–2176 (1992). [doi:10.1088/0264-9381/9/9/015](https://doi.org/10.1088/0264-9381/9/9/015)
48. L. L. Smarr, R. Blandford, The binary pulsar: Physical processes, possible companions, and evolutionary histories. *Astrophys. J.* **207**, 574 (1976). [doi:10.1086/154524](https://doi.org/10.1086/154524)
49. D. Lai, L. Bildsten, V. M. Kaspi, Spin-orbit interactions in neutron star/main-sequence binaries and implications for pulsar timing. *Astrophys. J.* **452**, 819 (1995). [doi:10.1086/176350](https://doi.org/10.1086/176350)
50. N. Wex, A timing formula for main-sequence star binary pulsars. *Mon. Not. R. Astron. Soc.* **298**, 67–77 (1998). [doi:10.1046/j.1365-8711.1998.01570.x](https://doi.org/10.1046/j.1365-8711.1998.01570.x)
51. S. Chandrasekhar, E. A. Milne, The highly collapsed configurations of a stellar mass. *Mon. Not. R. Astron. Soc.* **91**, 456–466 (1931). [doi:10.1093/mnras/91.5.456](https://doi.org/10.1093/mnras/91.5.456)
52. K. Boshkayev, H. Quevedo, B. Zhami, I –Love– Q relations for white dwarf stars. *Mon. Not. R. Astron. Soc.* **464**, 4349–4359 (2017). [doi:10.1093/mnras/stw2614](https://doi.org/10.1093/mnras/stw2614)
53. D. Foreman-Mackey, D. W. Hogg, D. Lang, J. Goodman, emcee: The MCMC Hammer. *PASP* **125**, 306–312 (2013). [doi:10.1086/670067](https://doi.org/10.1086/670067)
54. A. Gelman, D. B. Rubin, Inference from iterative simulation using multiple sequences. *Stat. Sci.* **7**, 457–472 (1992). [doi:10.1214/ss/1177011136](https://doi.org/10.1214/ss/1177011136)
55. S. R. Hinton, ChainConsumer. *J. Open Source Softw.* **1**, 45 (2016). [doi:10.21105/joss.00045](https://doi.org/10.21105/joss.00045)
56. N. I. Shakura, *Sov. Astron. Lett.* **11**, 224 (1985).
57. S.-C. Yoon, S. E. Woosley, N. Langer, Type Ib/c supernovae in binary systems. I. Evolution and properties of the progenitor stars. *Astrophys. J.* **725**, 940–954 (2010). [doi:10.1088/0004-637X/725/1/940](https://doi.org/10.1088/0004-637X/725/1/940)
58. T. M. Tauris, N. Langer, M. Kramer, Formation of millisecond pulsars with CO white dwarf companions. II. Accretion, spin-up, true ages and comparison to MSPs with He white

- dwarf companions. *Mon. Not. R. Astron. Soc.* **425**, 1601–1627 (2012). [doi:10.1111/j.1365-2966.2012.21446.x](https://doi.org/10.1111/j.1365-2966.2012.21446.x)
59. P. Lazarus, T. M. Tauris, B. Knispel, P. C. C. Freire, J. S. Deneva, V. M. Kaspi, B. Allen, S. Bogdanov, S. Chatterjee, I. H. Stairs, W. W. Zhu, Timing of a young mildly recycled pulsar with a massive white dwarf companion. *Mon. Not. R. Astron. Soc.* **437**, 1485–1494 (2014). [doi:10.1093/mnras/stt1996](https://doi.org/10.1093/mnras/stt1996)
60. T. M. Tauris, M. Kramer, P. C. C. Freire, N. Wex, H.-T. Janka, N. Langer, P. Podsiadlowski, E. Bozzo, S. Chaty, M. U. Kruckow, E. P. J. Heuvel, J. Antoniadis, R. P. Breton, D. J. Champion, Formation of double neutron star systems. *Astrophys. J.* **846**, 170 (2017). [doi:10.3847/1538-4357/aa7e89](https://doi.org/10.3847/1538-4357/aa7e89)
61. P. Ghosh, F. K. Lamb, Accretion by rotating magnetic neutron stars. III. Accretion torques and period changes in pulsating X-ray sources. *Astrophys. J.* **234**, 296 (1979). [doi:10.1086/157498](https://doi.org/10.1086/157498)
62. P. Ghosh, F. K. Lamb, “Diagnostics of disk-magnetosphere interaction in neutron star binaries,” in *X-Ray Binaries and the Formation of Binary and Millisecond Radio Pulsars*, E. P. J. van den Heuvel, S. A. Rappaport, Eds. (Springer, 1992), pp. 487–510.
63. D. Bhattacharya, E. P. J. van den Heuvel, Formation and evolution of binary and millisecond radio pulsars. *Phys. Rep.* **203**, 1–124 (1991). [doi:10.1016/0370-1573\(91\)90064-S](https://doi.org/10.1016/0370-1573(91)90064-S)
64. H.-T. Janka, Neutron star kicks by the gravitational tug-boat mechanism in asymmetric supernova explosions: progenitor and explosion dependence. *Astrophys. J.* **837**, 84 (2017). [doi:10.3847/1538-4357/aa618e](https://doi.org/10.3847/1538-4357/aa618e)